Extreme Mechanics Letters 55 (2022) 101799

Contents lists available at ScienceDirect

Extreme Mechanics Letters

journal homepage: www.elsevier.com/locate/eml

Biomechanical phenotyping of minuscule soft tissues: An example in the rodent tricuspid valve

William D. Meador [a], Mrudang Mathur [b], Sotirios Kakaletsis [c], Chien-Yu Lin [a], Matthew R. Bersi [d], Manuel K. Rausch [a,c,e,*]

[a] University of Texas at Austin, Department of Biomedical Engineering, 107 W Dean Keeton Street, Austin, 78712, TX, United States of America
[b] University of Texas at Austin, Department of Mechanical Engineering, 204 E Dean Keeton Street, Austin, 78712, TX, United States of America
[c] University of Texas at Austin, Department of Aerospace Engineering and Engineering Mechanics, 2617 Wichita Street, Austin, 78712, TX, United States of America
[d] Washington University in St. Louis, Department of Mechanical Engineering and Materials Science, 1 Brookings Drive, St. Louis, 63130, MO, United States of America
[e] University of Texas at Austin, Oden Institute for Computational Engineering and Sciences, 201 E 24th Street, Austin, 78712, TX, United States of America

ARTICLE INFO

Article history:
Received 3 April 2022
Received in revised form 19 May 2022
Accepted 25 May 2022
Available online 2 June 2022

Keywords:
Membrane
Bulge testing
Biaxial testing
Rat
Murine
Heart valve
Inverse analysis

ABSTRACT

The biomechanical phenotype of soft tissues – i.e., the sum of spatially- and directionally-varying mechanical properties – is a critical marker of tissue health and disease. While biomechanical phenotyping is always challenging, it is particularly difficult with minuscule tissues. For example, tissues from small animal models are often only millimeters in size, which prevents the use of traditional test methods, such as uniaxial tensile testing. To overcome this challenge, our current work describes and tests a novel experimental and numerical pipeline. First, we introduce a micro-bulge test device with which we pressurize and inflate minuscule soft tissues. We combine this micro-bulge device with an optical coherence tomography device to also image the samples during inflation. Based on pressure data and images we then perform inverse finite element simulations to identify our tissues' unknown material parameters. For validation, we identify the material parameters of a thin sheet of latex rubber via both uniaxial tensile testing and via our novel pipeline. Next, we demonstrate our pipeline against anterior tricuspid valve leaflets from rats. The resulting material parameters for these tissues compare excellently with data collected in sheep via standard planar biaxial testing. Additionally, we show that our device is compatible with other imaging modalities such as 2-Photon microscopy. To this end, we image the in-situ microstructural changes of the leaflets during inflation using second-harmonic generation imaging. In summary, we introduce a novel pipeline to biomechanically phenotype minuscule soft tissues and demonstrate its value by phenotyping the biomechanics of the anterior tricuspid valve leaflets from rats.

1. Introduction

The biomechanical phenotype of soft tissues – i.e., the sum of their spatially- and directionally-varying mechanical properties – is a critical indicator of tissue health, remodeling, and disease. A classic example of disease-induced alterations in biomechanical phenotype is the stiffening of arteries in patients with systemic hypertension [1]. Here, arterial stiffness – an intrinsic biomechanical property of arterial tissue – has become a valuable marker of disease progression and is strongly associated with the risk of adverse cardiovascular events [2,3]. Thus, the ability to reliably estimate the biomechanical phenotype of cardiovascular and other soft tissues is not only important to our basic scientific understanding of tissue function, but can also be integral to the clinical diagnosis, assessment, and management of disease progression [4–6].

Unfortunately, biomechanical phenotype cannot be easily cast into a single number, but is instead a complex set of nonlinear material properties [7–9]. Hence, biomechanical quantification often requires standardized tissue-specific testing methods and protocols. For example, multi-axial loading may be necessary to capture directionally-varying mechanical properties of tissues with a preferential microstructural organization [10]. Similarly, full-field measurement techniques may be necessary to

* Corresponding author at: University of Texas at Austin, Department of Aerospace Engineering and Engineering Mechanics, 2617 Wichita Street, Austin, 78712, TX, United States of America.
E-mail address: manuel.rausch@utexas.edu (M.K. Rausch).

https://doi.org/10.1016/j.eml.2022.101799
2352-4316/

capture spatially-varying mechanical properties and regions of tissue heterogeneity [11–14].

The biomechanics community has worked for decades to develop, test, and validate various biomechanical testing techniques and protocols for many types of soft tissues, beginning with the seminal work of Fung [15]. Given tissue accessibility at the time, most of these testing methods and protocols were initially developed for tissue from humans or large animal models, where sample dimensions are on the order of centimeters [16,17]. Indeed, such samples can be relatively easily handled, prepared for full-field imaging, mounted, and tested. However, given the recent advances in genomic and medical sciences, it is becoming increasingly evident that small animal models (i.e., rodents) are more important than ever in scientific research, noting that there are currently thousands of novel small animal disease models available for study [18–20]. To fully exploit such small animal models and better understand the biomechanical consequences of soft tissue remodeling and disease, standardized methods and protocols for biomechanical phenotyping of small animal soft tissues will have to be established.

Naturally, the translation of large animal testing approaches to biomechanical phenotyping of small animal tissues comes with significant challenges. The majority of these challenges are related to the tissues being minuscule; that is, tissue sizes on the scale of millimeters or smaller rather than centimeters. Others have used nanoindentation and similar methods to overcome the geometric challenges of biomechanical phenotyping minuscule soft tissues [21,22]. Their work has provided critical and unprecedented insight into the biomechanical phenotype of minuscule soft tissues. However, such methods are generally direction-agnostic and evoke deformation modes that do not mimic the in-vivo loading of soft tissues. Because of this non-physiological loading, such methods are not ideal for the quantification and study of the structure-function relationship of tissues, which is a critical element of biomechanical phenotyping [23]. Moreover, while some methods consider material anisotropy, they are often limited to linear elasticity [24], or quarter-symmetric specimen geometries [25]. For certain minuscule tissues, such as rodent arteries, others have developed standardized testing approaches that have been designed around constitutive modeling and biomechanical phenotyping [4]. For example, Bersi et al. have tested the arteries of mice in a miniature pressure-inflation device [26]. However, for membranous soft tissues such as fetal membranes, pericardium, skin, tympanic membrane, or heart valve tissue, no such testing methods exist. To overcome this technical gap, our current work introduces an experimental and numerical pipeline to biomechanically phenotype minuscule, thin membranous soft tissues under in-vivo loading conditions using a combination of bulge inflation, optical coherence tomography imaging, and inverse finite element modeling. Additionally, we show that our method is suitable for simultaneous in-situ microstructural characterization via 2-photon microscopy-based second harmonic generation imaging. Thus, our method allows for direct quantification of both structure and function in membranous soft tissues. We demonstrate the utility of the proposed method by performing a controlled validation with latex rubber prior to identification of the biomechanical phenotype of rodent anterior tricuspid valve leaflets.

2. Materials and methods

2.1. Animal model and sample excision

We performed all animal and experimental procedures with strict adherence to the Principles of Laboratory Animal Care, formulated by the National Society for Medical Research, and the Guide for Care and Use of Laboratory Animals prepared by the National Academy of Science and published by the National Institutes of Health. This animal use protocol was also approved by our local Institutional Animal Care and Use Committee (University of Texas at Austin). In our experiments, we sacrificed 6 Sprague-Dawley male rats (Taconic, Model # SD-M, Germantown, NY, USA), aged 10–12 weeks (354 ± 19 g) via carbon dioxide inhalation. To excise the tricuspid valve, we first extracted the hearts and performed a double atriotomy to expose the atrioventricular junctions. Next, we accessed the right ventricle via the pulmonary artery and opened the tricuspid annulus by cutting the anteroseptal commissure. Then, we isolated the tricuspid valve by cutting the papillary muscles free and trimming the leaflets free along the annulus. Once removed, leaflets were cryogenically stored at $-80\,^{\circ}$C in a 9:1 solution of DMEM:DMSO with protease inhibitor (Thermo Fisher Scientific, Catalog # A32953, Waltham, MA, USA) until testing, as previously described [27].

2.2. Description of micro-bulge device and sample mounting

To biomechanically phenotype minuscule soft tissues, we designed a custom micro-bulge test device. This device is made of clear acrylic and the overall construction is intentionally designed to fit under the optics of both our Optical Coherence Tomography (OCT) device (Thorlabs, Inc., Newton, NJ, USA) and our 2-Photon microscopes (Ultima IV, Bruker, Billerica, MA, US), see Fig. 1. The device has two Luer lock ports to attach a pressure transducer (PXM409, Omega Engineering, Norwalk, CT, USA) and a syringe pump (Legato 110, KD Scientific Inc, Holliston, MA, USA). Once the device is filled with room temperature deionized (DI) water, and air bubbles are removed, a PDMS gasket is placed above the inflation chamber. The gasket has a hole that matches the sample's test region. In our experiments, the test region was chosen such that we maintained approximately a 10:1 ratio in sample length to sample thickness (e.g., 1 mm diameter for rat tricuspid valve leaflet that has a thickness of approximately 100 μm). Next, we placed the sample on the gasket. After we positioned the sample, the top chamber was added and filled with water. We then placed the micro-bulge test device under either an OCT scanner (Section 2.4), or 2-Photon microscope (Section 2.5). Using a custom LabVIEW (LabVIEW Version 20.0.1, National Instruments, Austin, TX, USA) virtual instrument, we programmed the syringe pump to displace liquid at a test-specific rate until achieving the target pressure, as measured by the pressure transducer. For rat tricuspid valve leaflets, liquid was displaced at a rate of 0.025 mL/min until a pressure of 30 mmHg was reached. The specific test protocols are discussed in detail in Section 2.3 and the Supplementary Methods.

2.3. Tricuspid valve leaflet testing

We first thawed our tissue samples and isolated the anterior leaflet, carefully removing as much annular tissue and as many chordae tendineae as possible without damaging the leaflet. Next, we mounted our sample in the micro-bulge test device. While doing so, we made sure to align the radial and circumferential direction of the tissue with the principal axes of our device. Once mounted, we preconditioned the tissue with ten loading cycles to 30 mmHg at a syringe displacement rate of 0.025 mL/min. Note, this pressure range represents the physiological loading of the tricuspid valve in-vivo [28]. After preconditioning the tissue, we unmounted and remounted it to remove any tissue slack that may have resulted from preconditioning. After remounting, we manually applied a small pressure preload (1.51 ± 0.65 mmHg) to establish a slightly convex reference configuration (to avoid

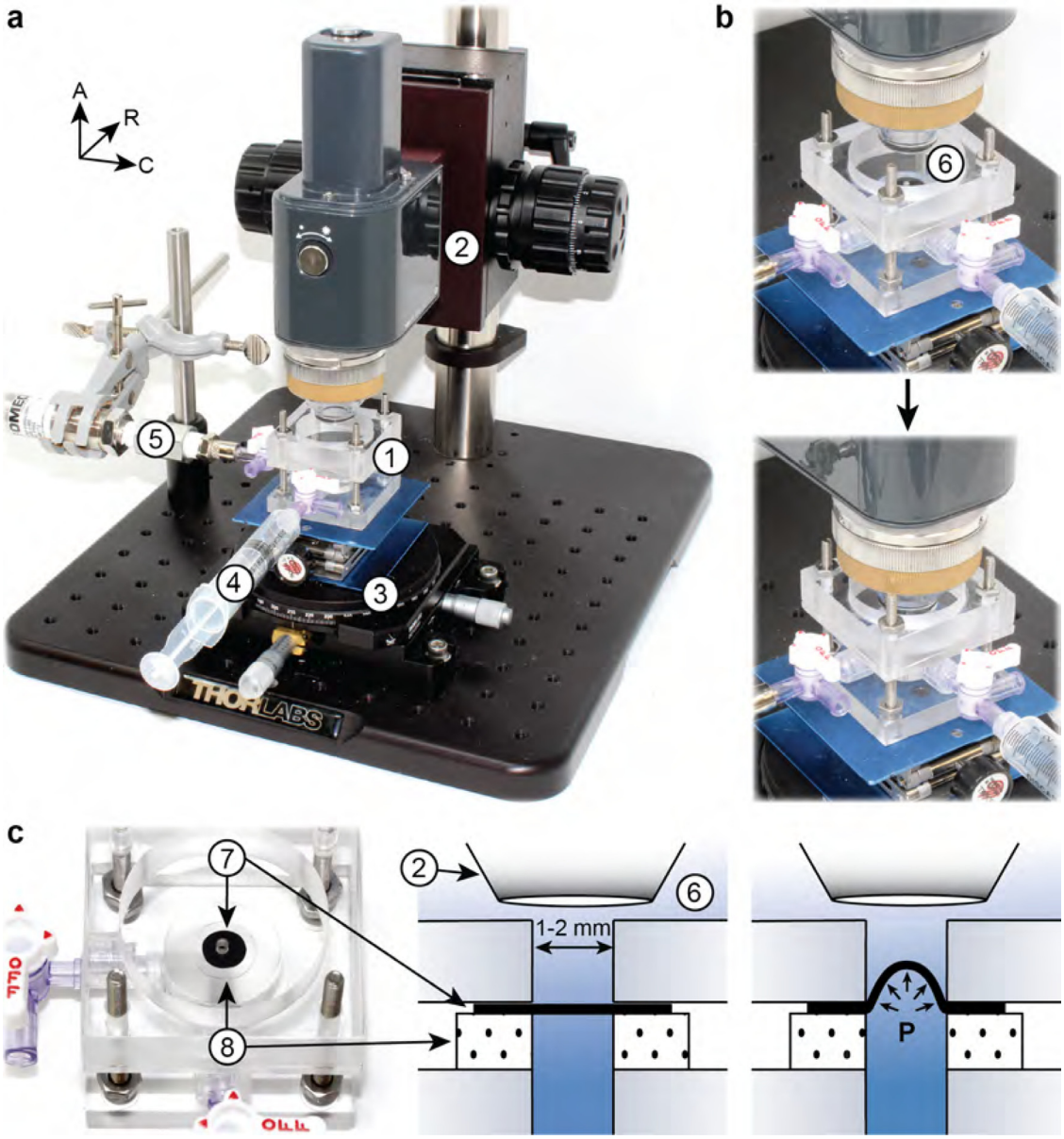

Fig. 1. Description of micro-bulge device. (a) Our micro-bulge test device (1) fits under either an optical coherence tomography (OCT) scanner (2) or a 2-Photon microscope (not shown). A micro-adjusting stage (3) allows for height adjustments. During testing, a syringe pump (4) pressurizes the device, as measured by a pressure transducer (5). (b) A water bath (6) sits on top of the test sample (7) for water immersion. (c) A PDMS gasket (8) seals the pressurized chamber during testing.

the snap-through instability during testing) and zeroed our pressure transducer. To capture the tissue's reference geometry, we performed a 3D OCT scan in this reference state, see Section 2.4. Next, we executed a single inflation to 30 mmHg during which we captured 2D OCT B-scans in the circumferential and radial directions of the tissue throughout loading at a rate of 5 images per second. After loading, we transferred the setup to the 2-Photon microscope for subsequent microstructural evaluation. Under the 2-Photon microscope, we returned the sample to the same reference state as before, with minimal pressurization to ensure a slightly convex reference geometry. Using the imaging protocol as described in Section 2.5, we imaged the collagen structure under Second Harmonic Generation imaging (SHG) with consecutive pressure increases to 0, 5, 10, 20, and 30 mmHg. Note, we held each pressure constant to allow for the finite imaging time of the 2-Photon microscope. We then analyzed these images for mean fiber angle and fiber distribution, see Section 2.5. Lastly, we fixed the tissue in 10% neutral buffered formalin for 24 h, and stored the leaflets in 70% ethanol until histological processing. Histology sections were stained with Movat Pentacrome and Picrosirius Red stains by a commercial service (HistoServ, Inc., Germantown, MD, USA).

2.4. Optical coherence tomography

We performed all OCT scans with a commercial OCT device (Telesto, ThorLabs, Inc., Newton, NJ, USA) with the ThorImage OCT software (Version 5.4.4). We acquired both 3D scans of the entire test region before micro-bulge inflation in a reference state, and simultaneous 2D scans of both radial and circumferential tissue directions throughout inflation. We assumed leaflet samples to have an index of refraction of 1.33, based on previous reports of similar collagenous tissues [29]. For 3D scans we acquired C-scans at (5.5 kHz) and a resolution of 512 × 216 × 373 pixels

(1.5 × 1.5 × 1.0 mm). At this resolution, acquisition time was 26 s per 3D scan. After imaging, we exported 3D scans to ImageJ (ImageJ Version 1.51, National Institutes of Health, Bethesda, MD, USA) for subsequent NRRD format conversion. Next, we manually segmented each sample's 3D volume in 3DSlicer (Version 4.11.20200930) [30] and exported the 3D geometry to MATLAB (MATLAB R2021a, MathWorks, Natick, MA, USA) in STL format. Within MATLAB, we averaged the top and bottom (i.e., atrialis and ventricularis) surfaces to acquire a mid-surface, which we used to inform our finite element geometry, see Section 2.6. Similarly, for 2D scans we acquired B-scans at (5.5 kHz) in a cross pattern, to simultaneously capture orthogonal planes of data (i.e., radial and circumferential directions of tissue). Note, we used 2D OCT during testing because of its significantly shorter imaging time and, therefore, higher sampling rate. After imaging, we exported the 2D scan data to MATLAB, where we used a custom code to algorithmically threshold the data and isolate the specimen from the background. After identifying the top and bottom surfaces, we averaged both curves to acquired the sample midline throughout the loading history. The resulting midline-pressure data subsequently informed our inverse finite element pipeline, see Section 2.6.

2.5. 2-Photon microscopy

Using a 20× water immersion objective (XLUMPLFLN, Olympus, Center Valley, PA, USA), we imaged a 450 × 450 μm region in the center of our tissue samples using SHG imaging [31]. Specifically, we epicollected the SHG signal from a 900 nm laser excitation with a 460 ± 25 nm photomultiplier tube channel filter at a 1024 × 1024 pixel resolution, ensuring full thickness acquisition of the central region at a step size of 10 μm. The imaging protocol was repeated while the micro-bulge device inflated the sample to 0, 5, 10, 20, and 30 mmHg. All images were processed in ImageJ, as previously reported [27]. In short, we first normalized each image's histogram based on saturation and applied median and minimum filters to reduce noise and enhance contrast. On these processed images we used the ImageJ plugin OrientationJ [32] to determine the fiber orientation distribution. Next, we fit a π-periodic von Mises probability distribution to the output distribution, $R(\theta)$, from OrientationJ, viz.

$$R(\theta) = \exp\left(b\cos\left(2[\theta-\alpha]\right)\right)/[2\pi I_0(b)] \tag{1}$$

where θ is the fiber angle, I_0 is the modified Bessel function, and α and b are the von Mises mean fiber angle and fiber concentration, respectively [33].

To also demonstrate the expanded utility of this device, we stained one tissue sample with Hoechst 33342 (Thermo Fischer Scientific, Catalog # H3570, Waltham, MA, USA) in staining buffer for 20 min to visualize and image cell nuclei at 800 nm laser excitation with a 460 ± 25 nm photomultiplier tube channel filter with the same imaging protocol as before, see Supplementary Figure 1.

2.6. Inverse finite element pipeline

To derive material parameters from our micro-bulge test data, we used an inverse finite element approach centering around Abaqus Standard 6.20-1 (Dassault Systems, Vélizy-Villacoublay, France), see Fig. 2a. To start with, we built the finite element model geometry from the 3D OCT data of the samples in the reference state, see Fig. 2b. Specifically, we first reduced the 3D OCT to its midline and imported this geometry to Coreform Cubit (Cubit 2020.2, Coreform LLC, Orem, UT, USA). In Cubit, we discretized this geometry with 1100 quadrilateral shell elements (convergence analysis provided in Supplementary Figure 2). Also note, we imaged and meshed the sample geometry beyond the test region including those parts of the sample that were compressed between the top plate and the gasket of the device. Then, we informed the referential shell thicknesses based on 3D OCT-derived heterogeneous thickness maps. Once the geometry was meshed, we applied zero-displacement boundary conditions to all nodes on the outer sample boundary. Next, we applied a compressive distributed surface load on elements outside the testing region due to the weight of the top plate of our device. Lastly, we applied the inflation pressure quasi-statically to the bottom surface of our samples across the test region. For the tricuspid valve tissue, we chose the anisotropic hyperelastic Holzapfel–Gasser–Ogden (HGO) material model [34], with parameters C_{10}, D, k_1, k_2, κ, and α, as implemented in Abaqus viz.

$$W(\mathbf{C}) = W_{dev.}(\bar{\mathbf{C}}) + W_{dil.}(J) \tag{2}$$

where

$$W_{dev.}(\bar{\mathbf{C}}) = C_{10}\left[\overline{I_1} - 3\right] + k_1/2k_2\left[\exp\left(k_2\left[\kappa\overline{I_1} + [1-3\kappa]\,\overline{I_4} - 1\right]^2\right) - 1\right] \tag{3}$$

and

$$W_{dil.}(J) = \left[\left[J^2/2 - 1\right]/2 - \ln J\right]/D \tag{4}$$

Here we decompose the deformation gradient $\mathbf{F}$ into a deviatoric, $\bar{\mathbf{F}} = J^{-1/3}\mathbf{F}$, and dilatational component, $J^{1/3}\mathbf{I}$, where $J = \det\mathbf{F}$. We then define the deviatoric right Cauchy–Green deformation tensor as $\bar{\mathbf{C}} = \bar{\mathbf{F}}^T\bar{\mathbf{F}}$. Furthermore, we define invariants $\overline{I_1} = \bar{\mathbf{C}} : \mathbf{I}$ and $\overline{I_4} = \bar{\mathbf{C}} : \mathbf{M}$ with $\mathbf{M}$ being the structural tensor, $\mathbf{M} = \mathbf{a}(\alpha) \otimes \mathbf{a}(\alpha)$, and $\mathbf{a}(\alpha)$ being the collagen mean fiber orientation vector.

For each simulation, we chose a bulk modulus ($K = 2/D$) so as to maintain a bulk modulus-to-shear modulus ratio of approximately 1000 at large strains. Further, we modeled a single fiber family at angle α and dispersion κ based on our 2-Photon data in the reference configuration [34]. Therefore, C_{10}, k_1, and k_2 were the only unknown material parameters to be identified via the nonlinear least squares regression. Note, C_{10} is frequently interpreted as the stiffness of the amorphous "ground substance" of soft tissues, while k_1 and k_2 are frequently interpreted as parameters associated with the stiffness of the collagen fibers. Finally, during the least squares fitting, we iterated on the unknown material parameters to minimize the error between the measured and the predicted midline geometry until convergence was reached. See Fig. 2c for an example of a converged analysis comparing the 2D OCT data with the respective finite element simulations.

3. Results

3.1. Validation of the micro-bulge test and inverse finite element pipeline

Before biomechanically phenotyping minuscule soft tissue using our micro-bulge device, we first validated our combined experimental and numerical pipeline, see Supplementary Figure 3. Specifically, we identified the mechanical properties of latex rubber using both, gold standard uniaxial tensile testing and our micro-bulge-based setup. All experimental and procedural details as well as an in-depth discussion of the results are provided in the Supplementary Methods and Results. We found generally excellent agreement between measurements via uniaxial tensile testing and our novel pipeline, see Supplementary Figure 4. Although, we did find a mean bias of −0.032 MPa, indicating that our device slightly overestimated the shear modulus as compared to uniaxial tension testing. In other words, samples behave slightly stiffer when tested in our setup than under uniaxial extension. However, this error falls well within the expected between-subject variation for soft tissues [23,35,36].

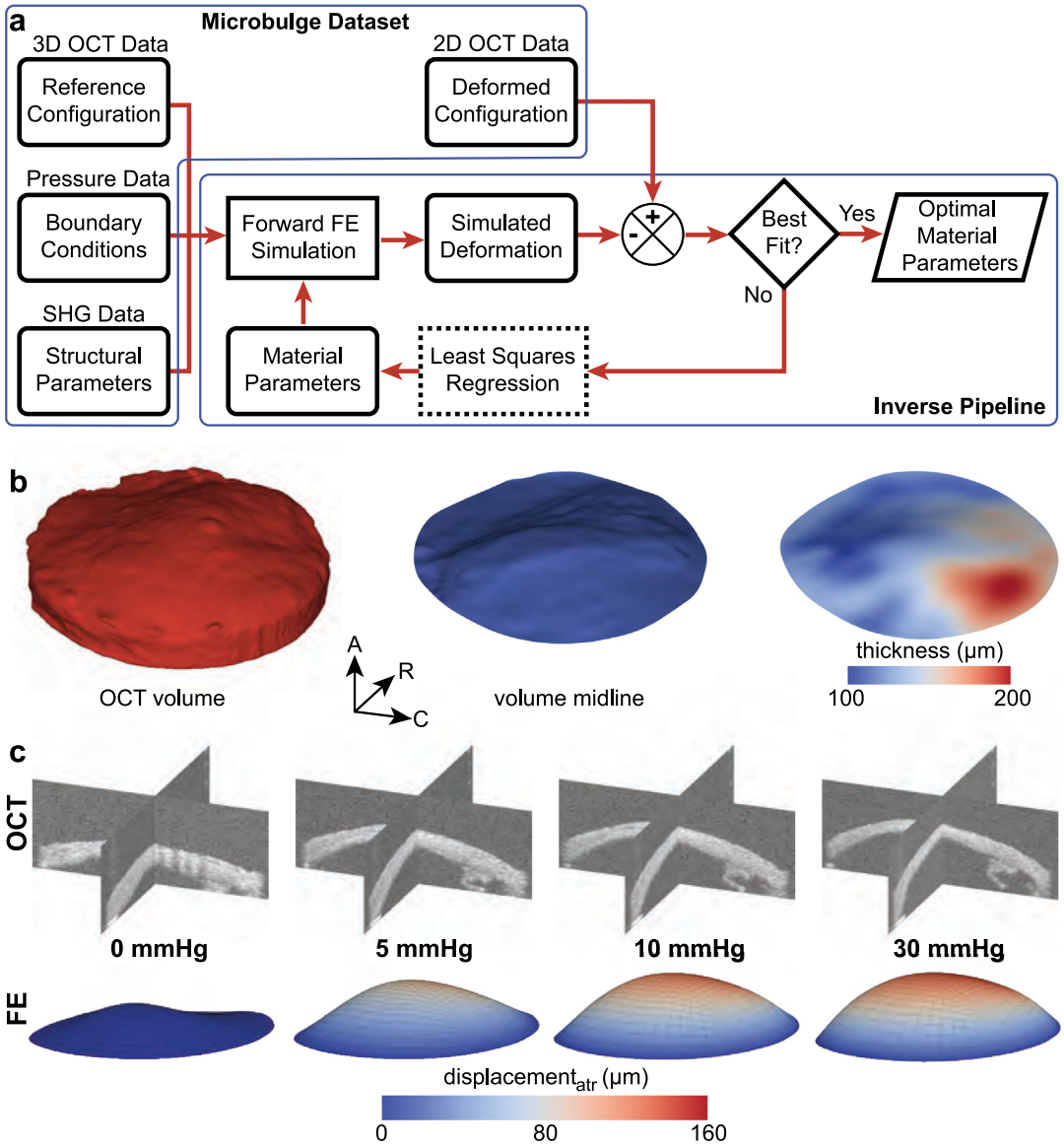

Fig. 2. Nonlinear least squares regression pipeline for biomechanical phenotyping of minuscule soft tissues. (a) Schematic showing that material parameters are inversely identified by minimizing the error between a (numerically) predicted material response to sample inflation and the experimentally measured material response using least squares regression. The numerical predictions are based on Finite Element (FE) simulations where Optical Coherence Tomography (OCT) data, pressure data, and 2-Photon-based Second-Harmonic Generation (SHG) structural data serve as model inputs. (b) Full volume of sample test region as measured via 3D OCT (left); the same volume reduced to its mid-surface (middle); and a heterogeneous thickness map representing the full volume (right). (c) Comparison between 2D OCT images along the radial and circumferential directions of anterior tricuspid valve leaflets under increasing inflation pressure and the corresponding (optimal) FE simulations.

3.2. Rodent tricuspid valve leaflets are a representative membranous soft tissue

In an effort to demonstrate our phenotyping pipeline with a minuscule biological tissue, we successfully isolated the tricuspid valve anterior leaflet from 6 Sprague-Dawley rats. Anatomically, we found many similar characteristics of these anterior leaflets to those from human [37] and large animal models [27], despite apparent size differences. That is, the gross tissue structure of the tricuspid valve is similar, with the valve having three leaflets, each attached to the tricuspid annulus. Additionally, chordae tendineae connect the leaflet's ventricularis to papillary muscles of the right ventricle (Fig. 3a). We also used histology to inspect the composition of rat tricuspid leaflets (Fig. 3b). From picrosirius red stains, we found that rat tricuspid valve leaflets are highly collagenous. Additionally, we identified abundant cell populations – both endothelial and interstitial – from Movat pentachrome staining. In the same stains, we also observed elastin fibers near the atrialis of the leaflets and small amounts of muscle fibers near the annulus. Lastly, trace amounts of glycosaminoglycans lie in the interstitial space of the leaflets. Together, these observations are consistent with other species' tricuspid valve leaflets and, more importantly, represent the general tissue structure of collagenous soft tissues; especially those with a membranous geometry. Thus, rodent tricuspid valve leaflets make an excellent model tissue that embodies the complexity of minuscule tissue biomechanical characterization.

3.3. Micro-bulge device lends itself to simultaneous evaluation of tissue structure and function

The goal of the current study is the comprehensive quantification of minuscule tissues' biomechanical phenotype, including

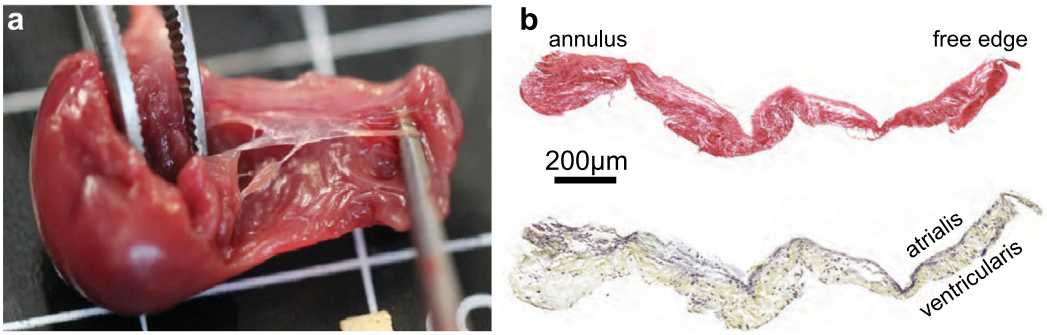

Fig. 3. Rat tricuspid valve anatomy, structure, and composition. (a) Rat tricuspid anterior leaflet, as shown in situ. Note the leaflet attachment to the annulus and the chordae tendinae attachments to the papillary muscles. (b) Histological thickness profile and composition of rat tricuspid valve leaflet as shown via picrosirius red (top) and Movat pentachrome (bottom) stains. Note, picrosirius red stains collagen red, while Movat pentachrome stains elastin blue/black, cells blue/black, collagen yellow, and muscle tissue red. (For interpretation of the references to color in this figure legend, the reader is referred to the web version of this article.)

their microstructure and the associated deformation under applied loads. Thus, we designed the micro-bulge device to be compatible with a 2-Photon microscope for stain-free SHG imaging of tissues' collagenous extracellular matrix under deformation. To demonstrate this capability, we imaged rat tricuspid valve leaflets under progressive micro-bulge inflation at pressures of 0, 5, 10, 20, and 30 mmHg. The results are shown in Fig. 4. In the inflation region of the tissue, we successfully imaged and analyzed the orientation distributions of collagen fibers (Fig. 4a). During testing, we qualitatively observed that there were relatively small changes in fiber direction (Fig. 4b), but a noticeable change in fiber concentration. To quantify these observations, we computed von Mises parameters of collagen fiber orientations throughout loading (Fig. 4c). We found that increasing pressure induced only small changes in the mean fiber angle between the initial (0 mmHg) and the loaded states. In fact, we observed only approximately 8° in angle change between 0 mmHg and 30 mmHg. Furthermore, it appears that most fiber angle rotation occurs within the first 10 mmHg of loading. Additionally, we observed a continued increase in fiber concentration toward the mean direction. This increase was most pronounced between 0 and 10 mmHg. Thus, while the mean fiber direction does not appear to rotate significantly during loading, individual fibers do rotate toward the mean fiber direction; thereby, increasing the fiber concentration.

3.4. Rodent tricuspid valve phenotype and inter-species comparison

Using our micro-bulge device, we successfully identified the biomechanical phenotype of rat tricuspid valve leaflets. That is, in addition to studying the valve's microstructure under loading as described in the previous paragraph, we also determined the tissue's material parameters as defined in the HGO hyperelastic constitutive law. Fig. 5a,b shows the stress and stretch fields from the final, converged nonlinear finite element solution to the micro-bulge boundary value problem. These data demonstrate both spatial heterogeneity and directional anisotropy. That is, stresses and stretches are non-uniform across the test region (further supporting the use of an inverse finite element pipeline) and they vary between the radial and circumferential directions. The identified material parameters are summarized in Table 1. When these parameters are applied to the homogeneous biaxial boundary value problem, they predict a material behavior that closely resembles our planar biaxial data previously collected on sheep tricuspid valve leaflets, see Fig. 5c; that is, an anisotropic, strain-stiffening material.

Table 1
Constitutive parameters for Holzapfel–Gasser–Ogden model. Parameters μ, k_1, and k_2 fit via inverse finite element analysis, and parameters α and κ informed via 2-Photon microscopy.

Sample	μ (MPa)	k_1 (MPa)	k_2(−)	α (°)	κ(−)	RMSE (mm)
1	4.84e−3	2.44e−4	30.51	−37.21	0.18	3.91e−2
2	9.55e−3	2.50e−4	14.23	−47.97	0.14	4.97e−2
3	5.03e−3	1.91e−4	132.01	−34.12	0.12	2.19e−2
4	6.65e−3	1.98e−4	128.16	−77.13	0.19	2.60e−2
5	2.97e−3	2.23e−4	6.63	−81.37	0.25	6.24e−2
6	4.61e−3	3.29e−5	19.76	−66.15	0.13	4.62e−2

4. Discussion

Biomechanical phenotyping of collagenous soft tissues is an important task. For example, we have recently shown that tricuspid valve disease leads to, and may be exacerbated by, fibrotic tissue stiffening and thickening [38]. Thus, biomechanically phenotyping patients' tricuspid valves may be of diagnostic and prognostic value. Unfortunately, biomechanical phenotyping is also a formidable task due to these tissues' complex mechanical behavior that is spatially- and directionally-dependent. This complexity arises from these tissues' often complex hierarchical, anisotropic, and heterogeneous (micro-)structures. This task is further complicated as the tissues shrink in size such as in studies with rodents. In this work, we set out to develop a testing system and numerical pipeline that can be used to reliably measure the biomechanical properties of minuscule, membranous, soft tissues using rodent tricuspid valve leaflets as a proof of concept.

To this end, we designed, validated, and demonstrated a micro-bulge-based test pipeline. We designed our combined experimental, imaging, and numerical pipeline to holistically evaluate the tissue under interrogation. That is, we biomechanically phenotype not only the materials' mechanical behavior, but also the sources of its behavior including its heterogeneous thickness distribution and microstructural organizations using in-situ OCT imaging and 2-Photon microscopy, respectively. For our test mode, we chose bulge testing, as it mimics the in-vivo biaxial loading of many membranous soft tissues including the heart valve leaflets [39].

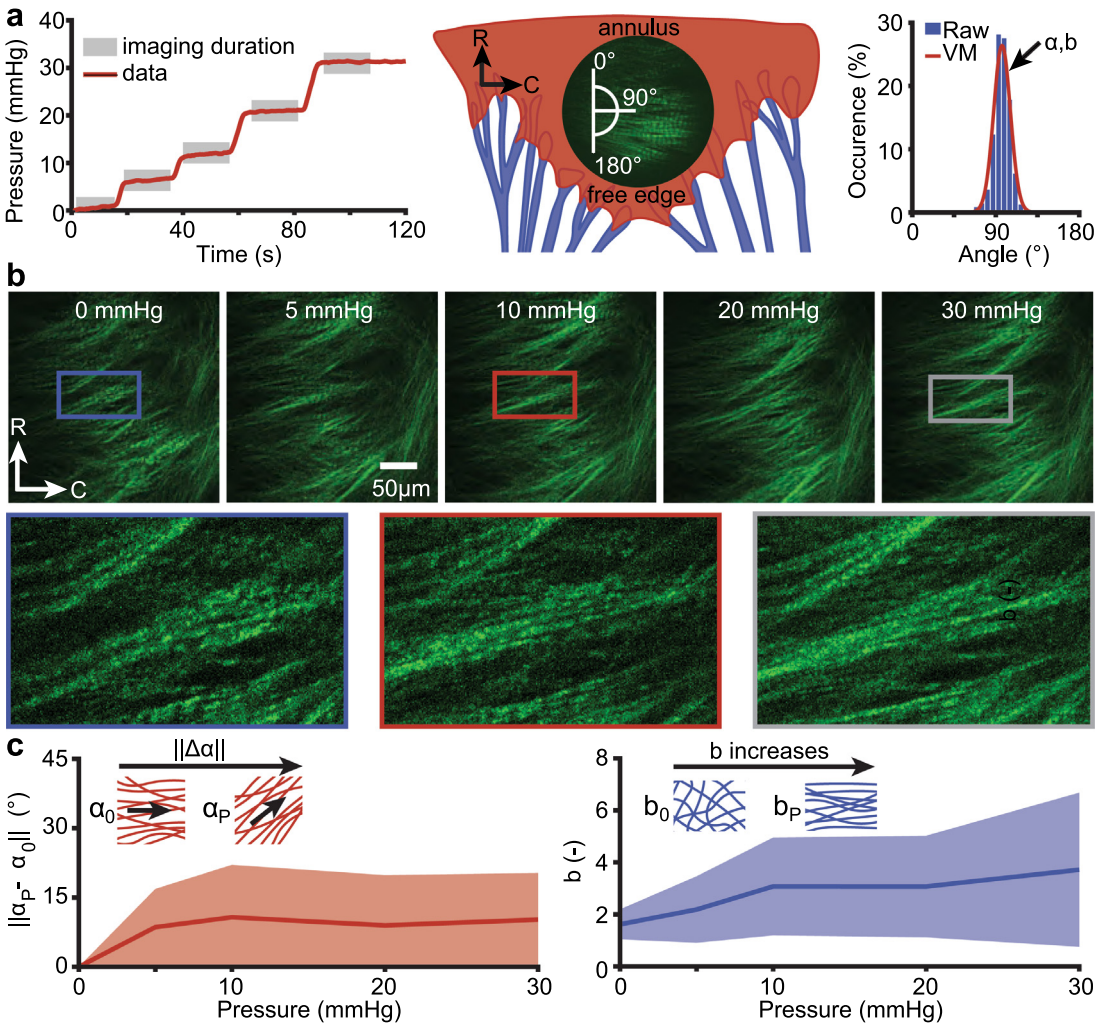

Fig. 4. Micro-bulge testing of rat tricuspid valve leaflets under 2-Photon microscopy. (a) Tricuspid leaflets under increasing inflation pressure between 0 mmHg and 30 mmHg (left). Each loading step is followed by a wait period during which we captured (gray bar) second harmonic generation images of the sample via 2-Photon microscopy. Depiction of a rat tricuspid leaflet with the testing region and the radial (R) as well as circumferential (C) directions (middle). In each second harmonic generation image, we quantified collagen orientation by fitting von Mises distributions to the raw fiber orientation distributions to identify the distribution parameters α and b — representing the mean fiber orientation and fiber concentration, respectively (right). (b) Representative images of the same tissue region with progressively increased pressures (panels represent 5:1 zoom-ins). (c) Change in fiber orientation mean angle (left, n=6) and change in fiber concentration (n=6) with increasing pressure (right). Data shown as means ± one standard deviation.

As a first step, we validated our pipeline against uniaxial tensile testing on a relatively simple material: latex rubber. We found minor discrepancies between testing modalities, the causes for which could be multi-fold, but are likely related to the physical constraints of bulge testing versus the free lateral constraints of uniaxial tensile testing. Especially with very small samples, boundary effects may have an impact on our results by artificially stiffening the material response. For example, we confirmed that mounting the samples induces small prestrains (on the order of 5%) near the sample boundaries, see Supplementary Figure 5. In larger samples, increasing the test area may reduce the impact of such spurious effects. However, in minuscule soft tissues this is an intrinsic limitation of the sample size. Nonetheless, given the generally large variations in soft tissue properties due to between-subject and even within-subject variations, we consider our reported bias small and an acceptable error.

In a next step, we ensured through structural and histological studies that the rodent tricuspid valve leaflets were, in fact, an appropriate model system for minuscule soft tissues. Note, in-vivo the tricuspid valve undergoes complex mechanical loading that is comprised of bending, tension, shear, and compression modes [39]. In response to these biomechanical and mechanobiological demands, its leaflets have biologically evolved complex micro- and macro-structure. In brief, we found rodent tricuspid valve leaflets to be highly collagenous, but also composed of cells, elastin, and glycosaminoglycans. We found these constituents to be highly organized in multiple layers whose relative thickness and cell population varies across the valve. These findings match those of other species' tricuspid valve leaflets very well [27,40]. Additionally, these compositional and (micro-)structural characteristics represent the broad class of membraneous soft tissues and are therefore an appropriate model system for our study.

Finally, we applied our biomechanical phenotyping pipeline to rodent tricuspid valve leaflets. Each element of our pipeline could be successfully executed on these minuscule tissues whose lateral dimensions are approximately 2 mm and whose thickness is on average approximately 100 μm. That is, we successfully mounted the tissue and imaged it under 3D OCT based on which we were able to map out the tissue's heterogeneous thickness distribution. Additionally, we were able to image its collagenous microstructure via stain-free SHG imaging in response to pressure loading. Finally, our inverse finite element analysis successfully converged for each tested sample yielding the parameters of

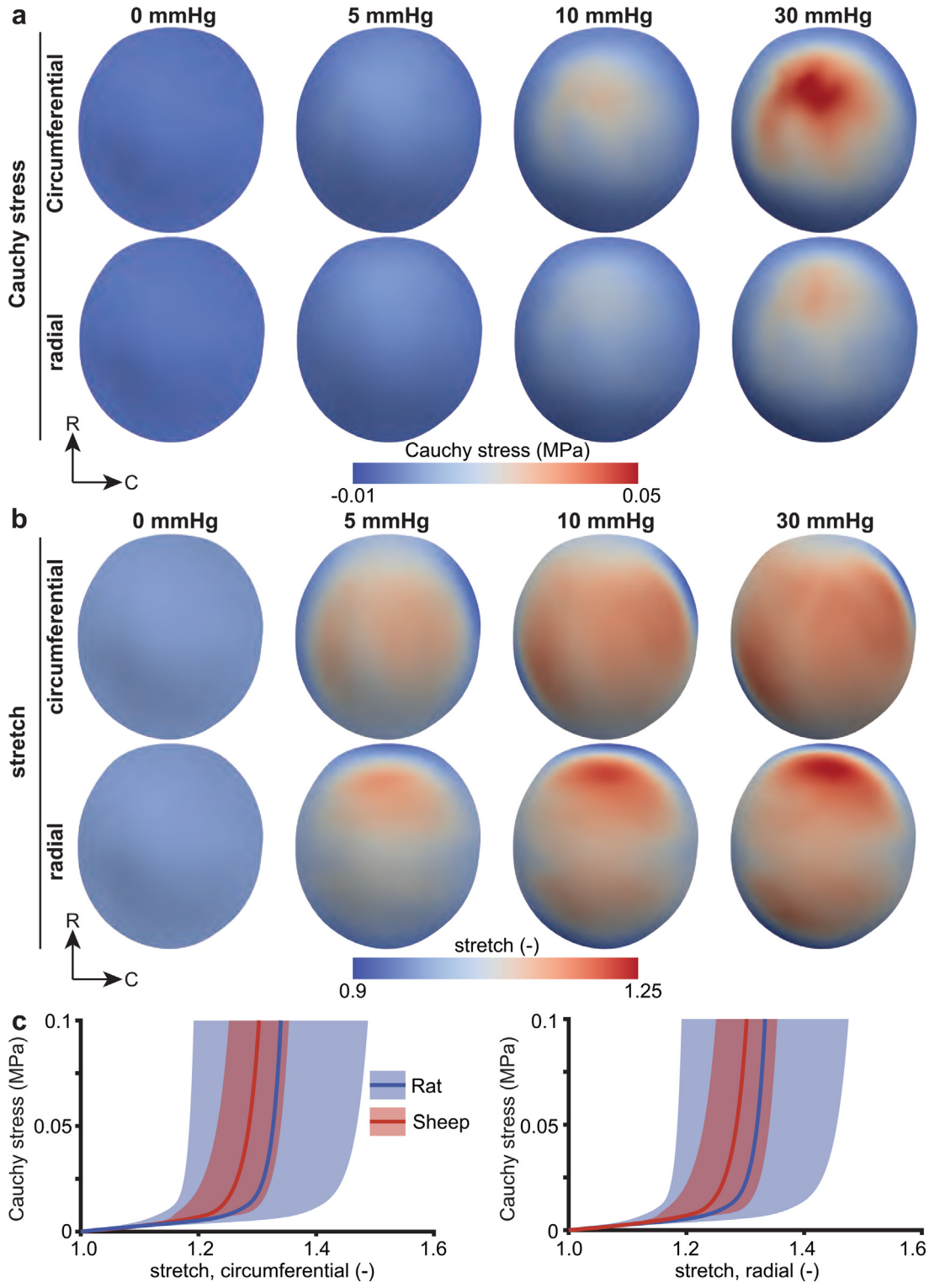

Fig. 5. Biomechanical phenotyping results from rat tricuspid valve leaflet micro-bulge inflation. (a) Cauchy stress in circumferential and radial directions at pressures between 0 mmHg and 30 mmHg. (b) Stretch in circumferential and radial direction at pressures between 0 mmHg and 30 mmHg. (c) Comparison between the constitutive behavior of rat tricuspid valve leaflets (results from this work) against data in sheep; both in circumferential direction (left) and radial direction (right).

the HGO hyperelastic material model. While not the focus of our study, our in-situ SHG images additionally revealed some of the known mechanisms that contribute to the strain-stiffening behavior of many collagenous materials. That is, we showed that under initial loading the collagenous microstructure of our target tissue first engaged in fiber re-orientation and concentration before "locking" and stiffening, giving rise to the traditional J-shape of soft tissues' mechanical response. Together, these data provide a comprehensive set of biomechanical phenotyping parameters that not only include thickness, (micro-)structure, and constitutive model parameters, but also reveal the structure-function relationship of this tissue. Note, we also found that the biomechanical phenotype of rodent tricuspid valve leaflets matches that of sheep very well. This is an important form of validation for

our inverse pipeline given that the structure and composition of both species leaflets are similar and should thus lead to similar biomechanical phenotypes.

4.1. Limitations and potential concerns

Naturally, our study suffers from limitations and potential concerns. Most importantly, we ignored some tissue complexities when building the finite element models of our soft tissue samples. For example, we did not include any spatial heterogeneity in the microstructural organization of the tissue. That is, we assumed that collagen fibers are equally oriented and dispersed throughout the tissue. While this is certainly not true, we have previously found a relatively small variation in mean fiber direction of 17° across the center of the tissue [27], and thus anticipate the potential impact of this simplification being small. Similarly, we ignored our samples' through-thickness heterogeneity in composition and structure. Here again, we acknowledge this simplification but expect that the practical implications are minimal. This is especially true as we ensured that our region of interest laid in the "belly" of the leaflet that shows a high degree of homogeneity as compared to the other leaflet regions [27]. Nonetheless, these are limitations in the inverse modeling approach and do not indicate limitations of the proposed micro-bulge testing device. Finally, we ignored the time-dependent, i.e., viscoelastic, behavior of our tissue. It is well-known that soft tissue behaves viscoelastically [41]. To reduce the complexity of our protocol and modeling pipeline, we ignored this behavior and preconditioned our tissue to minimize its effects [42]. Please note, however, that neither our experimental nor numerical procedure is prohibitive of including viscoelasticity. Additionally, the high spatial resolution of our imaging modalities (order of micrometers), the rigidity of our bulge tester apparatus, and the easy interchangeability of the pressure transducers, render our device (and pipeline) appropriate for a wide size range and stiffness range of tissues. In summary, our limitations and potential concerns are all focused on simplifications we made in the analysis of our tissue and are not limitations of our setup. Future studies that are specifically concerned with the biomechanical phenotype of rodent tricuspid valves, or other similar tissues, can use the exact same set-up with added complexities to quantify the impact of microstructural- and through-thickness heterogeneity and the importance of including viscoelasticity in the modeling pipeline.

4.2. Conclusion

In conclusion, we developed, validated, and tested an experimental and numerical pipeline to biomechanically phenotype minuscule soft tissues. To this end, we combined a micro-bulge test device, with in-situ OCT and 2-Photon microscopy, and an inverse finite element pipeline. We demonstrated its usefulness by biomechanically phenotyping rodent tricuspid valve leaflets and successfully reporting their heterogeneous thickness map, the in-situ deformation of their collagenous microstructure, and tissue-specific material parameters as defined in an established hyperelastic material model for soft tissue. While a side-product of our work, we thereby also found that rodent tricuspid valve leaflets behave very similarly to those of sheep. Importantly, the findings from the current study can be extended to many membranous soft tissues – such as rodent heart valve leaflets, fetal membranes, or pericardium – that cannot be quantified using standard mechanical testing approaches. Furthermore, the combination of imaging modalities and inverse finite element modeling has the potential to extend this testing framework to incorporate more complex material models accounting for viscoelasticity and geometric variations. Together, our work will hopefully inform and inspire others that aim at biomechanically phenotyping minuscule soft tissues.

Declaration of competing interest

The authors declare the following financial interests/personal relationships which may be considered as potential competing interests: Manuel Rausch reports a relationship with Edwards Lifesciences that includes: speaking and lecture fees.

Acknowledgments

We acknowledge the support by the National Institutes of Health, United States of America through a predoctoral fellowship to Dr. Meador (F31HL145976) and research award to Dr. Bersi (R00HL146951). Additionally, we acknowledge support by the American Heart Association, United States of America through awards to Dr. Rausch (18CDA34120028) and a predoctoral fellowship to Mrudang Mathur (902502).

Disclosures

Manuel K. Rausch has a speaking agreement with Edwards Lifesciences. None of the other authors have conflicts of interest to disclose.

Appendix A. Supplementary data

Supplementary material related to this article can be found online at https://doi.org/10.1016/j.eml.2022.101799.

References

[1] Z. Sun, Aging, arterial stiffness, and hypertension, Hypertension 65 (2) (2015) 252–256.
[2] J. Vappou, J. Luo, E.E. Konofagou, Pulse wave imaging for noninvasive and quantitative measurement of arterial stiffness in vivo, Am. J. Hypertens. 23 (4) (2010) 393–398.
[3] G.F. Mitchell, S.-J. Hwang, R.S. Vasan, M.G. Larson, M.J. Pencina, N.M. Hamburg, J.A. Vita, D. Levy, E.J. Benjamin, Arterial stiffness and cardiovascular events: the framingham heart study, Circulation 121 (4) (2010) 505–511.
[4] J. Ferruzzi, M. Bersi, J. Humphrey, Biomechanical phenotyping of central arteries in health and disease: advantages of and methods for murine models, Ann. Biomed. Eng. 41 (7) (2013) 1311–1330.
[5] H.N. Hayenga, B.C. Thorne, S.M. Peirce, J.D. Humphrey, Ensuring congruency in multiscale modeling: towards linking agent based and continuum biomechanical models of arterial adaptation, Ann. Biomed. Eng. 39 (11) (2011) 2669–2682.
[6] S. Liu, G. Bao, Z. Ma, C.J. Kastrup, J. Li, Fracture mechanics of blood clots: Measurements of toughness and critical length scales, Extrem. Mech. Lett. 48 (2021) 101444.
[7] B. Spronck, J.D. Humphrey, Arterial stiffness: Different metrics, different meanings, J. Biomech. Eng. 141 (9) (2019) 1–12, http://dx.doi.org/10.1115/1.4043486.
[8] A. Anssari-Benam, D.L. Bader, H.R.C. Screen, A combined experimental and modelling approach to aortic valve viscoelasticity in tensile deformation, J. Mater. Sci.: Mater. Med. 22 (2) (2011) 253–262, http://dx.doi.org/10.1007/s10856-010-4210-6.
[9] A. Srivastava, A.B. Tepole, C.-Y. Hui, Skin stretching by a balloon tissue expander: Interplay between contact mechanics and skin growth, Extrem. Mech. Lett. 9 (2016) 175–187.
[10] M.S. Sacks, Biaxial mechanical evaluation of planar biological materials, J. Elasticity Phys. Sci. Solids 61 (1) (2000) 199–246.
[11] M. Palanca, G. Tozzi, L. Cristofolini, The use of digital image correlation in the biomechanical area: A review, Int. Biomech. 3 (1) (2016) 1–21.
[12] M.R. Bersi, C. Bellini, P. Di Achille, J.D. Humphrey, K. Genovese, S. Avril, Novel methodology for characterizing regional variations in the material properties of murine aortas, J. Biomech. Eng. 138 (7) (2016) 071005.
[13] C.M. Luetkemeyer, L. Cai, C.P. Neu, E.M. Arruda, Full-volume displacement mapping of anterior cruciate ligament bundles with dualmri, Extrem. Mech. Lett. 19 (2018) 7–14.
[14] Y. Zhou, C. Gong, G.S. Lewis, A.D. Armstrong, J. Du, 3D full-field biomechanical testing of a glenoid before and after implant placement, Extrem. Mech. Lett. 35 (2020) 100614.

[15] Y. Fung, Elasticity of soft tissues in simple elongation, Am. J. Physiol.-Legacy Content 213 (6) (1967) 1532–1544.
[16] J. Humphrey, D. Vawter, R. Vito, Quantification of strains in biaxially tested soft tissues, J. Biomech. 20 (1) (1987) 59–65, http://dx.doi.org/10.1016/0021-9290(87)90267-3.
[17] T.K. Tonge, L.S. Atlan, L.M. Voo, T.D. Nguyen, Full-field bulge test for planar anisotropic tissues: Part I – experimental methods applied to human skin tissue, Acta Biomater. 9 (4) (2013) 5913–5925, http://dx.doi.org/10.1016/j.actbio.2012.11.035.
[18] D. Chen, M.-W. Wang, Development and application of rodent models for type 2 diabetes, Diabetes, Obes. Metab. 7 (4) (2005) 307–317.
[19] J.A. Diaz, P. Saha, B. Cooley, O.R. Palmer, S.P. Grover, N. Mackman, T.W. Wakefield, P.K. Henke, A. Smith, B.K. Lal, Choosing a mouse model of venous thrombosis: A consensus assessment of utility and application, Arteriosclerosis, Thromb. Vasc. Biol. 39 (3) (2019) 311–318.
[20] Z.-Q. Liu, X. Zhang, J.F. Wenk, Quantification of regional right ventricular strain in healthy rats using 3D spiral cine dense MRI, J. Biomech. 94 (2019) 219–223.
[21] M. Oyen, Nanoindentation of biological and biomimetic materials, Exp. Tech. 37 (1) (2013) 73–87.
[22] M.-K. Sewell-Loftin, C.B. Brown, H.S. Baldwin, W.D. Merryman, A novel technique for quantifying mouse heart valve leaflet stiffness with atomic force microscopy, J. Heart Valve Dis. 21 (4) (2012) 513–520.
[23] S. Kakaletsis, W.D. Meador, M. Mathur, G.P. Sugerman, T. Jazwiec, M. Malinowski, E. Lejeune, T.A. Timek, M.K. Rausch, Right ventricular myocardial mechanics: Multi-modal deformation, microstructure, modeling, and comparison to the left ventricle, Acta Biomater. 123 (2021) 154–166.
[24] D. Chaparro, V. Dargam, P. Alvarez, J. Yeung, I. Saytashev, J. Bustillo, A. Loganathan, J. Ramella-Roman, A. Agarwal, J.D. Hutcheson, A method to quantify tensile biaxial properties of mouse aortic valve leaflets, J. Biomech. Eng. 142 (10) (2020) http://dx.doi.org/10.1115/1.4046921.
[25] J.E. Bischoff, E.S. Drexler, A.J. Slifka, C.N. McCowan, Quantifying nonlinear anisotropic elastic material properties of biological tissue by use of membrane inflation, Comput. Methods Biomech. Biomed. Eng. 12 (3) (2009) 353–369, http://dx.doi.org/10.1080/10255840802609420.
[26] M. Bersi, R. Khosravi, A. Wujciak, D. Harrison, J. Humphrey, Differential cell-matrix mechanoadaptations and inflammation drive regional propensities to aortic fibrosis, aneurysm or dissection in hypertension, J. R. Soc. Interface 14 (136) (2017) 20170327.
[27] W.D. Meador, M. Mathur, G.P. Sugerman, T. Jazwiec, M. Malinowski, M.R. Bersi, T.A. Timek, M.K. Rausch, A detailed mechanical and microstructural analysis of ovine tricuspid valve leaflets, Acta Biomater. 102 (2020) 100–113, http://dx.doi.org/10.1016/j.actbio.2019.11.039.
[28] M.K. Rausch, M. Malinowski, W.D. Meador, P. Wilton, A. Khaghani, T.A. Timek, The effect of acute pulmonary hypertension on tricuspid annular height, strain, and curvature in sheep, Cardiovasc. Eng. Technol. 9 (3) (2018) 365–376, http://dx.doi.org/10.1007/s13239-018-0367-9.
[29] A. Jannasch, C. Schnabel, R. Galli, S. Faak, P. Büttner, C. Dittfeld, S.M. Tugtekin, E. Koch, K. Matschke, Optical coherence tomography and multiphoton microscopy offer new options for the quantification of fibrotic aortic valve disease in ApoE-/- mice, Sci. Rep. 11 (1) (2021) 1–14.
[30] R. Kikinis, S.D. Pieper, K.G. Vosburgh, 3D slicer: A platform for subject-specific image analysis, visualization, and clinical support, in: Intraoperative Imaging and Image-Guided Therapy, Springer, 2014, pp. 277–289.
[31] P.J. Campagnola, A.C. Millard, M. Terasaki, P.E. Hoppe, C.J. Malone, W.A. Mohler, Three-dimensional high-resolution second-harmonic generation imaging of endogenous structural proteins in biological tissues, Biophys. J. 82 (1) (2002) 493–508.
[32] R. Rezakhaniha, A. Agianniotis, J.T.C. Schrauwen, A. Griffa, D. Sage, C.v. Bouten, F. Van De Vosse, M. Unser, N. Stergiopulos, Experimental investigation of collagen waviness and orientation in the arterial adventitia using confocal laser scanning microscopy, Biomech. Model. Mechanobiol. 11 (3) (2012) 461–473.
[33] A.J. Schriefl, A.J. Reinisch, S. Sankaran, D.M. Pierce, G.A. Holzapfel, Quantitative assessment of collagen fibre orientations from two-dimensional images of soft biological tissues, J. R. Soc. Interface 9 (76) (2012) 3081–3093.
[34] T.C. Gasser, R.W. Ogden, G.A. Holzapfel, Hyperelastic modelling of arterial layers with distributed collagen fibre orientations, J. R. Soc. Interface 3 (6) (2006) 15–35.
[35] K. Smith, M. Mathur, W. Meador, B. Phillips-Garcia, G. Sugerman, A. Menta, T. Jazwiec, M. Malinowski, T. Timek, M. Rausch, Tricuspid chordae tendineae mechanics: insertion site, leaflet, and size-specific analysis and constitutive modelling, Exp. Mech. 61 (1) (2021) 19–29.
[36] G.P. Sugerman, S. Kakaletsis, P. Thakkar, A. Chokshi, S.H. Parekh, M.K. Rausch, A whole blood thrombus mimic: Constitutive behavior under simple shear, J. Mech. Behav. Biomed. Mater. 115 (2021) 104216.
[37] M. Silver, J. Lam, N. Ranganathan, E. Wigle, Morphology of the human tricuspid valve, Circulation 43 (3) (1971) 333–348.
[38] W.D. Meador, M. Mathur, G.P. Sugerman, M. Malinowski, T. Jazwiec, X. Wang, C.M. Lacerda, T.A. Timek, M.K. Rausch, The tricuspid valve also maladapts as shown in sheep with biventricular heart failure, Elife 9 (2020) e63855.
[39] M.S. Sacks, A.P. Yoganathan, Heart valve function: A biomechanical perspective, Philos. Trans. R. Soc. B 362 (1484) (2007) 1369–1391, http://dx.doi.org/10.1098/rstb.2007.2122, arXiv:34547608816.
[40] K.E. Kramer, C.J. Ross, D.W. Laurence, A.R. Babu, Y. Wu, R.A. Towner, A. Mir, H.M. Burkhart, G.A. Holzapfel, C.-H. Lee, An investigation of layer-specific tissue biomechanics of porcine atrioventricular valve anterior leaflets, Acta Biomater. 96 (2019) 368–384.
[41] G.A. Holzapfel, et al., Biomechanics of soft tissue, Handb. Mater. Behav. Models 3 (1) (2001) 1049–1063.
[42] Y.-C. Fung, Biomechanics: Mechanical Properties of Living Tissues, Springer Science & Business Media, 2013.